Hadronic vacuum polarization contribution to the muon $g-2$ with $(2+1)$-flavor lattice QCD on a larger than $(10\ \mathrm{fm})^4$ lattice at the physical point

Eigo Shintani,[1] and Yoshinobu Kuramashi[2]

(PACS Collaboration)

[1] *RIKEN Center for Computational Science, Kobe, Hyogo 650-0047, Japan*
[2] *Center for Computational Sciences, University of Tsukuba, Tsukuba, Ibaraki 305-8577, Japan*

(Received 6 February 2019; published 27 August 2019)

We study systematic uncertainties in the lattice QCD computation of the hadronic vacuum polarization (HVP) contribution to the muon $g-2$. We investigate three systematic effects: the finite volume (FV) effect, the cutoff effect, and integration scheme dependence. We evaluate the FV effect at the physical pion mass on two different volumes of $(5.4\ \mathrm{fm})^4$ and $(10.8\ \mathrm{fm})^4$ using the PACS10 configurations at the same cutoff scale. For the cutoff effect, we compare two types of lattice vector operators, which are local and conserved (point-splitting) currents, by varying the cutoff scale on a larger than $(10\ \mathrm{fm})^4$ lattice at the physical point. For the integration scheme dependence, we compare the results between the coordinate- and momentum-space integration schemes at the physical point on a $(10.8\ \mathrm{fm})^4$ lattice. Our result for the HVP contribution to the muon $g-2$ is given by $a_\mu^{\mathrm{hvp}} = 737(9)(^{+13}_{-18}) \times 10^{-10}$ in the continuum limit, where the first error is statistical and the second one is systematic.

DOI: 10.1103/PhysRevD.100.034517

I. INTRODUCTION

The muon anomalous magnetic moment $(g-2)_\mu$ has been a key observable for a proof of predictability of quantum field theory. We expect that there might be a sign of the new physics beyond the standard model (BSM) in the muon $g-2$ anomaly, which is 3σ to 4σ deviation between the standard model (SM) prediction and the BNL experiment [1,2] suggested in 2004. In order to establish that the $(g-2)_\mu$ experiments in FermiLab and J-PARC [3,4] aiming at a factor of 4 to 5 improvement from the BNL experiment is forthcoming. However, the high precision experiments are not sufficient for the search of the BSM physics [5] since the magnitude of theoretical uncertainty in the SM prediction has not been comparable to that in the new experiments yet. The biggest uncertainty left in the SM prediction is coming from the hadronic vacuum polarization (HVP) effect, which is the leading order of the hadronic contribution to $(g-2)_\mu$ denoted by a_μ^{hvp}. The phenomenological estimate of a_μ^{hvp} [6–11], which has been employed in the SM prediction, is obtained by the integrated hadronic R-ratio measured in an e^+e^- annihilation experiment. Including several hadronic decay channels with a particular choice of the center-of-mass energy $\sqrt{s}$ window, in which the perturbative QCD is used for $\sqrt{s} \simeq 2$ GeV, a_μ^{hvp} is phenomenologically estimated at a 0.4% level of precision [12].

Lattice QCD (LQCD) is another approach to estimate a_μ^{hvp} totally independent of the phenomenological estimate. This is a theoretical calculation based on the first principle of QCD, whereas the current precision of the LQCD estimate is roughly an order of magnitude lower than the phenomenological one, and it then does not satisfy accuracy to search the BSM physics (see a recent review [13] and the references therein). The main difficulty of the LQCD calculation is that, in the Euclidean space-time, the detailed behavior of the HVP contribution with high precision is required around the peak position of the QED kernel, which is significantly below the hadronic scale of Λ_{QCD}. In such a low-energy region, corresponding to a long distance in the coordinate space-time, it is not an easy task to make a high precision measurement of the HVP contribution because of the exponentially diminishing signal-to-noise ratio in a deeply infrared regime.

In addition, the contribution of the ρ resonance state decreases in this regime, while two-pion or three-pion state contributions, which are possible decay modes of the vector resonance, become prominent. This means that a sufficiently large volume at the physical point, where the ρ resonance has an open threshold and the multipion states are allowed, is required in the LQCD calculation to correctly estimate the HVP contribution. Furthermore, it is imperative for LQCD to take account of the cutoff effect to obtain a_μ^{hvp} in the continuum limit. So the LQCD determination of a_μ^{hvp} at a subpercent precision is still a challenging task.

Recent LQCD calculations [14–18] are carried out with the aid of an estimate of effective models, for instance, the chiral perturbation theory (ChPT) [19–21] or the Gounaris-Sakurai (GS) parametrization [13,15], to correct the finite volume (FV) effect on $(\lesssim 6\ \mathrm{fm})^3$ boxes at a long distance. In Ref. [17], the leading-order ChPT estimate is added to the lattice result on a $(5.4\ \mathrm{fm})^3$ box at the physical pion mass taking higher-order contributions of $\mathcal{O}(p^4)$ as a systematic error. Reference [16] employs a similar strategy to add the ChPT estimate to the lattice results on $(6.1-6.6\ \mathrm{fm})^3$ lattices around the physical pion mass but takes the systematic error conservatively. In Ref. [15], the GS parametrization is used to fit the LQCD result of the vector correlator on a roughly $(4\ \mathrm{fm})^3$ lattice at the unphysical pion mass ($m_\pi \geq 185$ MeV) with the time-slice cut of $1.1 < t_{\mathrm{cut}} < 1.4$ fm. References [14,18] take account of only the two-pion contributions based on the analytic estimate with ChPT.

As pointed out in our previous study [22], it is essentially important to assess the FV effect in the LQCD calculation of a_μ^{hvp} by employing the direct comparison between different volumes at the physical pion mass without any reliance on the effective models. We have made a direct evaluation of the systematic uncertainty of the FV effect using different volumes of $(8.1\ \mathrm{fm})^3$ and $(5.4\ \mathrm{fm})^3$ near the physical pion mass ($m_\pi = 135$–145 MeV). The difference between the results on two volumes was found to be larger than the ChPT estimate, though the statistical error was so large that they are consistent within 1σ error bar. In this article, we perform a more precise comparison with ChPT using a lattice larger than $(10\ \mathrm{fm})^4$ at the physical pion mass, which are a subset of the PACS10 configurations [23] generated by the PACS Collaboration. We also investigate the lattice cutoff effect by comparing the results at two different cutoffs of $a^{-1} = 2.33$ and 3.09 GeV keeping the physical volume larger than $(10\ \mathrm{fm})^4$. We finally estimate an extrapolated value of a_μ^{hvp} in the continuum limit and compare it with other recent LQCD results.

This paper is organized as follows. In Sec. II, we explain the notation and the LQCD methodology to calculate a_μ^{hvp}. Lattice parameters and numerical method are explained in Sec. III. The results for the FV effect and the lattice cutoff effect are presented in Secs. IV A and IV B, respectively. In Sec. IV C, we numerically check the consistency between the results with the coordinate and momentum integration schemes. In Sec. IV D, we discuss our result in comparison with the phenomenological estimate and other recent LQCD results. The conclusion and an outlook are summarized in Sec. V.

II. METHODOLOGY

A. Momentum-space integration scheme

a_μ^{hvp} is given by the integral of the vacuum polarization function (VPF) $\Pi(Q^2)$ from zero to infinity in terms of the spacelike momentum squared $Q_{\mathrm{M}}^2 = -Q^2 < 0$:

$$a_\mu^{\mathrm{hvp}} = \left(\frac{\alpha_e}{\pi}\right)^2 \int_0^\infty dQ^2 K_E(Q^2)\hat{\Pi}(Q), \tag{1}$$

$$\hat{\Pi}(Q) \equiv \Pi(Q) - \Pi(0), \tag{2}$$

$$K_E(s) = \frac{1}{m_\mu^2}\hat{s}Z^3(\hat{s})\frac{1-\hat{s}Z(\hat{s})}{1+\hat{s}Z^2(\hat{s})}, \tag{3}$$

$$Z(\hat{s}) = -\frac{\hat{s}-\sqrt{\hat{s}^2+4\hat{s}}}{2\hat{s}}, \qquad \hat{s} = \frac{s}{m_\mu^2}, \tag{4}$$

where $\hat{\Pi}(Q)$ is scheme independent due to a subtraction of scheme-dependent $\Pi(0)$. The QED kernel $K_E(s)$, which is obtained by the one-loop perturbation with $\alpha_e = 1/137.03599914$ and $m_\mu = 105.6583745$ MeV [24], has a sharp peak at $Q^2 \approx (\sqrt{5}-2)m_\mu^2 = 0.003\ \mathrm{GeV}^2$, and a rapid falloff for $Q^2 \to 0$. The vacuum polarization function can be extracted from a factorization of the vacuum polarization tensor $\Pi_{\mu\nu}(Q)$, which is given by the Fourier transformation of the vector-vector current correlator,

$$\Pi_{\mu\nu}(Q) \equiv \sum_x e^{iQx}\langle V_\mu^\Gamma(x)V_\nu^{\Gamma'}(0)\rangle = (Q^2\delta_{\mu\nu} - Q_\mu Q_\nu)\Pi(Q), \tag{5}$$

where the index Γ in the superposition of the vector current V_μ denotes two choices of lattice operators. One is the local current with $\Gamma' = \mathrm{L}$,

$$V_\mu^{\mathrm{L}}(x) = Z_V\bar{q}(x)\gamma_\mu q(x), \tag{6}$$

with Z_V being the renormalization constant, and the other is the conserved current with $\Gamma = \mathrm{C}$,

$$V_\mu^{\mathrm{C}}(x) = \frac{1}{2}[\bar{q}(x+a\hat{\mu})(1+\gamma_\mu)U_\mu^\dagger(x)q(x) - \bar{q}(x)(1-\gamma_\mu)U_\mu(x)q(x+a\hat{\mu})], \tag{7}$$

in the point-splitting form with the link variable $U_\mu(x)$, which preserves the lattice Ward-Takahashi identity $\sum_\mu \nabla^*_\mu V_\mu = 0$ with the backward differential $\nabla^*(x,y) = \delta_{x,y} - \delta_{x-\hat{\mu},y}$ in the naive Wilson quark action. Note that the lattice local vector current and conserved current are not $\mathcal{O}(a)$ improved in this study. In Sec. IV B, we investigate the scaling violation for both currents.

The expression of $\Pi_{\mu\nu}(Q)$ in Eq. (5) has extra contributions of $\mathcal{O}((aQ)^n)$ with $n \geq 2$ due to the Lorentz symmetry breaking on the discretized space-time in LQCD. After subtracting these lattice artifacts [25–27], $\hat{\Pi}(Q^2)$ computed with LQCD is consistent with the perturbative representation of the Adler function [28] in high $Q^2 > 1$ GeV^2 except for the nonperturbative objects such as the d-dimensional operator condensate term given by $\langle O_d \rangle / Q^{2d}$ appearing in the operator product expansion (OPE) [29]. For the actual computation of $a_\mu^{\rm hvp}$, the LQCD evaluation of the integral of Eq. (1) can be replaced by the perturbative one in the high Q^2 region from some particular point of $Q^2_{\rm PQCD}$ to infinity. Practically, the integrand for $Q^2_{\rm PQCD} > 1$ GeV^2 in Eq. (1) gives a minor contribution to the total $a_\mu^{\rm hvp}$ so that the OPE contribution should be negligible. We will discuss it later.

In LQCD, we need to evaluate $\Pi(0)$ by the extrapolation of VPF to the zero-momentum limit. Since the minimum momentum in LQCD is defined as $Q_{\rm min} = 2\pi/L$, a large volume allows us to perform the qualified extrapolation with less uncertainty of fitting procedures. Once $\Pi(0)$ is determined, the momentum integral of Eq. (1) is straightforwardly performed with the extrapolation function in the low-energy regime, and we can add the perturbative QCD formula in the high-energy regime of $Q^2 > Q_{\rm PQCD}$. As pointed out above, the choice of $Q^2_{\rm PQCD} > 1$ GeV^2 gives only a minor contribution to the total $a_\mu^{\rm hvp}$.

In our analysis, the Q^2 integral of Eq. (1) is split into the fit region, the lattice data region, and the perturbative QCD (PQCD) region:

$$\begin{aligned}[a_\mu^{\rm hvp}]_{\rm Mom} = &\int_0^{Q^2_{\rm fit}} dQ^2 W_q(Q^2)\hat{\Pi}_f(Q) \\ &+ \frac{1}{2}\sum_{Q_n^2=Q^2_{\rm fit}}^{Q_n^2<Q^2_{\rm PQCD}} (W_q(Q^2_{n+1})\hat{\Pi}_{\rm lat}(Q_{n+1}) \\ &+ W_q(Q_n^2)\hat{\Pi}_{\rm lat}(Q_n))(Q^2_{n+1} - Q_n^2) \\ &+ \int_{Q^2_{\rm PQCD}}^\infty dQ^2 W_q(Q^2)\hat{\Pi}_{\rm PQCD}(Q), \end{aligned} \tag{8}$$

$$W_q(s) \equiv \left(\frac{\alpha_e}{\pi}\right)^2 K_E(s), \tag{9}$$

$$\hat{\Pi}_{\rm lat}(Q) = \Pi_{\rm lat}(Q) - \Pi(0), \tag{10}$$

where we define the lattice momentum $Q_n = 2\pi n/L$ with integer $n = \{0, 1, \ldots, L/a - 1\}$, and $\hat{\Pi}_{\rm PQCD}$ is an analytic form in PQCD. $\hat{\Pi}_f(s) \equiv \Pi_f(s) - \Pi(0)$ is a functional form with the fitting ansatz, which is used for the extrapolation of the lattice data to obtain $\Pi(0)$. We utilize three types of fitting functions,

$$(\text{Padé ansatz}) \quad \Pi_f^{\rm Pade[1,1]}(s) = \Pi(0) + \frac{sX_0}{s+X_1}, \tag{11}$$

$$\Pi_f^{\rm Pade[2,1]}(s) = \Pi(0) + \frac{sX_0}{s+X_1} + sX_2, \tag{12}$$

$$(\text{Linear approx}) \quad \Pi_f^{\rm linear}(s) = \Pi(0) + sY, \tag{13}$$

with the fitting parameters $\Pi(0)$, X_0, X_1 X_2. Note that we use the same form of Padé approximation as in Refs. [15,30].

B. Coordinate-space integration scheme

As an alternative approach, we consider the vector-vector current correlator in the coordinate space:

$$C(x) = \sum_\mu \langle V_\mu(x) V_\mu(0)\rangle, \tag{14}$$

where the summation over the same component of sink and source vector currents is taken. With the use of $C(x)$, $a_\mu^{\rm hvp}$ can be expressed as follows[1]:

$$\begin{aligned} a_\mu^{\rm hvp} = &\left(\frac{\alpha_e}{\pi}\right)^2 \int d^4x C(x) \int_0^\infty d\omega^2 K_E(\omega^2) \frac{4\pi^2}{3\omega^2}\left[e^{iQx} - 1 \right.\\ &\left.\left. - \frac{\omega^2}{2}\lim_{\varepsilon^2=0}\left\{\sum_{\mu\nu}(-x_\mu x_\nu)\frac{\varepsilon^2}{P_\mu P_\nu}\right|_{P_\mu\neq 0, P_\nu\neq 0, \varepsilon=|P|}\right\}\right]_{\omega=|Q|}. \end{aligned} \tag{15}$$

Here there is a degree of freedom for a choice of four components in the momentum Q_μ satisfying $Q^2 = \omega^2$. If we take one component as nonzero and others as zero, i.e., $Q_\mu = \{Q_\rho = |Q|, Q_{\mu\neq\rho} = 0\}$, $\rho = \{x, y, z, t\}$, Eq. (15) is simplified as

$$\begin{aligned} a_\mu^{\rm hvp} = &\left(\frac{\alpha_e}{\pi}\right)^2 \int dx_\rho \bar{C}_\rho(x_\rho) \int_0^\infty d\omega^2 K_E(\omega^2)\frac{4\pi^2}{\omega^2} \\ &\times \left[e^{i\omega x_\rho} - 1 + \frac{\omega^2 x_\rho^2}{2}\right], \end{aligned} \tag{16}$$

where we define

[1] See the Appendix for the derivation.

TABLE I. Summary of the lattice parameters for the gauge field configurations used in this work.

	Refs.	L/a [L]	T/a [T]	a^{-1} (GeV)	m_π (MeV)	# configs.
PACS10	[23]	128 [10.8 fm]	128 [10.8 fm]	2.333(18)	135	21
		160 [10.3 fm]	160 [10.3 fm]	3.087(30)	135	40[a]
	[22,23]	64 [5.4 fm]	64 [5.4 fm]	2.333(18)	139	187
	[22]	64 [5.4 fm]	128[b] [10.8 fm]	2.333(18)	139	86

[a]Four rotational degrees of freedom are taken into account. Originally ten configurations were generated.
[b]64^4 gauge configurations are copied in the temporal direction, extending T/a to 128.

$$\bar{C}_\rho(x_\rho) = \sum_{\mu\neq\rho}\int\left(\prod_{\sigma\neq\rho}dx_\sigma\right)\langle V_\mu(x)V_\mu(0)\rangle. \quad (17)$$

This is a formula called time-momentum representation (TMR) [31], in particular, with the choice of the time direction for x_ρ.[2] It is consistent with the Lorentz-covariant coordinate-space representation [32] if the coordinate-space integral in Eq. (15) is transformed into the spherical and radial integrals.

In LQCD, we perform a discretized coordinate-space summation of the correlator on the finite lattice volume defined as

$$[a_\mu^{\rm hvp}]_{\rm lat}(r_{\rm cut}) = \frac{1}{2}\sum_{r/a=0}^{r_{\rm cut}/a-1}[C^{\Gamma\Gamma'}(r)W_r(r) + C^{\Gamma\Gamma'}(r+a)W_r(r+a)], \quad (18)$$

$$W_r(r) = 8\alpha_e^2\int_0^\infty\frac{d\omega}{\omega}K_E(\omega^2)[\omega^2r^2 - 4\sin^2(\omega r/2)] \quad (19)$$

with

$$C^{\Gamma\Gamma'}(x) = \sum_\mu\langle V_\mu^\Gamma(x)V_\mu^{\Gamma'}(0)\rangle, \quad (20)$$

where r, which denotes a distance from the source point, is regarded as the generalized expression of x_ρ in Eq. (16), and thus $C^{\Gamma\Gamma'}(r)$ represents $\bar{C}_\rho(x_\rho)$ on the lattice. This procedure introduces the systematic uncertainties due not only to the discretized summation but also to the truncation at some finite distance $r_{\rm cut}$.[3]

As we will explain below, the lattice used in this study is symmetric, and its spatial/temporal extension is large enough to control the finite volume effect and the backward propagation state (BPS) effect investigated in Ref. [22]. We can perform the integral of Eq. (16) [summation of Eq. (18)] for each direction of $\rho = x, y, z, t$, which allows us to increase the statistics by 4 times without much computational cost.

[2]We will not call "TMR" for Eq. (17), alternatively saying "coordinate-space representation" since the word "time" may be confusing.

[3]On the lattice, since the momentum is discretized, the momentum integral in Eq. (19) should be replaced as the summation of lattice momentum squared of $\omega^2 = \sum_\mu(2\pi n_\mu/L_\mu)^2$ for $n_\mu = [0, L_\mu - 1]$, while we naively use the momentum integral as the continuum. This assumption may also introduce additional systematic uncertainty, but taking the continuum limit and infinite volume limit will not be a concern.

III. CALCULATION DETAILS

A. Configurations

We use two subsets of the PACS10 configurations, which are generated with the stout-smeared $\mathcal{O}(a)$-improved Wilson-clover quark action and Iwasaki gauge action [33] on 128^4 and 160^4 lattices (the spatial extension L and temporal extension T are symmetric) at $\beta = 1.82$ and 2.00, respectively. In addition, we also employ the gauge field configurations on a 64^4 lattice at $\beta = 1.82$, which are copied in the temporal direction extending T/a to 128 in the FV study. Lattice parameters for these configuration sets are summarized in Table I. We investigate the FV effect using the 128^4 and 64^4 lattices at the same lattice spacing, and the study of the cutoff effect uses the 128^4 and 160^4 lattices with the fixed physical volume.

The detailed description of the configuration generation on the 128^4 and 64^4 lattices was already given in Ref. [23]. Here we explain the configuration generation on the 160^4 lattice at $\beta = 2.00$. We employ the stout-smearing parameter $\rho = 0.1$, and the number of the smearing steps is 6, which are the same as in the case of the 128^4 lattice at $\beta = 1.82$ [23]. The improvement coefficient of $c_{\rm SW} = 1.02$ is nonperturbatively determined by the Schrödinger functional (SF) scheme following Ref. [34]. The hopping parameters for the light (degenerate up-down) and strange quarks $(\kappa_{\rm ud}, \kappa_{\rm s}) = (0.125814, 0.124925)$ are carefully adjusted to yield the physical pion and kaon masses $(m_\pi, m_K) = (135.0\ {\rm MeV}, 497.6\ {\rm MeV})$ with the use of the cutoff of $a^{-1} = 3.09$ GeV ($a = 0.064$ fm) [35] determined from the Ξ mass $m_\Xi = 1.3148$ GeV. The hopping parameter for the charm (only valence quark) is set to $\kappa_c = 0.110428$ on 128^4 lattice, and $\kappa_c = 0.11452$ on 160^4 lattice adjusted to the physical point.

The degenerate up-down (ud) quarks are simulated with the domain-decomposed hybrid Monte Carlo (DDHMC) algorithm [36,37] on the 160^4 lattice. The ud quark determinant is separated into the UV and infrared (IR) parts after the even-odd preconditioning. We also apply the twofold mass preconditioning [38,39] to the IR part by splitting it into $\tilde{F}_{\mathrm{IR}}$, F'_{IR}, and F''_{IR}. This decomposition is controlled by two additional hopping parameters: $\kappa'_{\mathrm{ud}} = \rho_1\kappa_{\mathrm{ud}}$ with $\rho_1 = 0.9997$ and $\kappa''_{\mathrm{ud}} = \rho_1\rho_2\kappa_{\mathrm{ud}}$ with $\rho_2 = 0.9940$. $\tilde{F}_{\mathrm{IR}}$ is derived from the action preconditioned with κ'_{ud}. The ratio of two preconditioners with κ'_{ud} and κ''_{ud} gives F'_{IR}. F''_{IR} is from the heaviest preconditioner with κ''_{ud}. In the end, the force terms consist of the gauge force F_{g}, the UV force F_{UV}, and the three IR forces F''_{IR}, F'_{IR}, and $\tilde{F}_{\mathrm{IR}}$. The IR forces are obtained with the mixed precision nested BiCGStab method for the quark solver [40]. We adopt the multiple timescale integration scheme [41] in the MD steps. The associated step sizes are controlled by a set of integers $(N_0, N_1, N_2, N_3, N_4)$: $\delta\tau_{\mathrm{g}} = \tau/N_0N_1N_2N_3N_4$, $\delta\tau_{\mathrm{UV}} = \tau/N_1N_2N_3N_4$, $\delta\tau''_{\mathrm{IR}} = \tau/N_2N_3N_4$, $\delta\tau'_{\mathrm{IR}} = \tau/N_3N_4$, $\delta\tilde{\tau}_{\mathrm{IR}} = \tau/N_4$ with $\tau = 1.0$. Our choice of $(N_0, N_1, N_2, N_3, N_4) = (8, 2, 2, 2, 20)$ for the 160^4 lattices results in 82% acceptance rates. The strange quark is simulated with the RHMC algorithm [42] by choosing the force approximation range of $[\min, \max] = [0.000190, 1.90]$ with $N_{\mathrm{RHMC}} = 10$, and $\delta\tau_{\mathrm{s}} = \delta\tau''_{\mathrm{IR}}$ for the step size.

The renormalization constant Z_V for the local vector current operator in Eq. (6) depends on the lattice cutoff scale. We obtain $Z_V = 0.95153(76)$ at $a^{-1} = 2.33$ GeV ($\beta = 1.82$) with the SF scheme [43], and $Z_V = 0.9673(19)$ at $a^{-1} = 3.09$ GeV ($\beta = 2.00$) from the nucleon form factor. Note that we observe good consistency between the results of Z_V determined by the SF scheme and the nucleon form factor [44]. The physical observables are measured at every ten trajectories on 128^4 and 64^4, and every five trajectories on 160^4. The statistical error is estimated by the jackknife analysis with 1, 4, and 5 jackknife bin sizes for the 128^4, 160^4, and 64^4 lattices, respectively [23].

B. AMA with deflated SAP preconditioning

The precision of the light flavor vector-vector current correlator in the IR regime, which is the small Q^2 region in Eq. (1) or the long distance region from the source location in Eq. (18), has the vital importance to achieve a less than 1% level of accuracy for a_μ^{hvp} with LQCD. As in the previous study [22], we utilize the optimized all-mode-averaging (AMA) technique [45–47] to make an efficient calculation of the vector-vector current correlator in LQCD. For the AMA approximation [22,47], we use the parameter set illustrated in Table II. As shown in Refs. [22,47], the combination of AMA with the deflated Schwartz alternative procedure (SAP) preconditioning [48] achieves the remarkable performance on the large lattice, and it then allows us a precise calculation of a_μ^{hvp}, especially in a long distance region. In fact, the

TABLE II. The parameter of the AMA approximation on the 64^4, 128^4, and 160^4 lattices. The "SAP domain" column denotes the size of the SAP domain, and the "Deflation" column denotes the number of deflation fields on the deflated SAP preconditioning. "Iteration" denotes the stopping iteration of the general conjugate residual (GCR) method.

Quark	Lattice	SAP domain	Deflation	Iteration
Light	64^4	4^4	30	5
	128^4	8^4	50	7
	160^4	10^4	50	7
Strange	128^4	8^4	46	5
	160^4	10^4	30	5

condition number in the AMA method with the deflated SAP preconditioning does not have large volume dependence [22] since the low mode is effectively eliminated by the projection with a deflation field so that the computational cost to solve the light quark propagator does not increase even if the lattice size is enlarged. Although the computational cost of generation of deflation fields is increased in a large lattice size, it takes only a few percent of the total computational cost [22] in deflated SAP preconditioning. This provides us with another advantage to avoid consuming large storage space to save the low-lying mode.

In the left panel of Fig. 1, we show the volume scaling for the relative error of the correlator at the physical pion mass. This is more robust test of volume scaling than the previous study [22], where there might be possible contamination due to the pion mass difference between two volumes. From this plot, one can see that the ratio of the relative error between the 64^4 and 128^4 lattices has a consistent behavior with the expected scaling value of $\sqrt{64^3/128^3}$ in a long distance region $t \gtrsim 1.5$ fm, which means that the use of a large volume can significantly reduce the statistical error, especially for the IR regime. As illustrated in the right panel of Fig. 1, we also observe the universal behavior for the relative error of the vector-vector current correlator at different cutoff scales on the same physical volume. This feature is also expected from the volume scaling hypothesis for the statistical error.

C. Multihadron state contributions

Using our large lattice ensembles at the physical pion mass, the multihadron state contributions, mostly the two-pion state, are correctly involved in the vector-vector current correlator. Figure 2 plots the effective mass of the vector-vector current correlator with $(\Gamma, \Gamma') = (\mathrm{L}, \mathrm{C})$ on each ensemble. The ρ meson is allowed to decay into the energetic pions on those ensembles, since the two-pion state energy $2\sqrt{m_\pi^2 + (2\pi/L)^2}$ is much lower than the ρ meson mass $m_\rho = 770$ MeV. We observe that the effective mass goes down below 770 MeV around $t \approx 1$ fm and stays

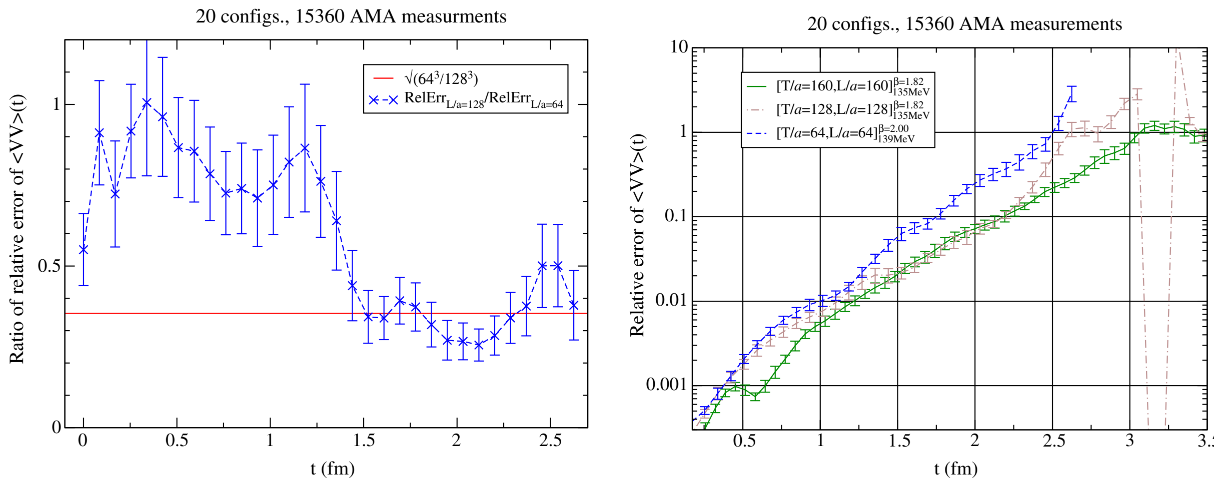

FIG. 1. (Left panel) Ratio of relative error for the vector-vector current correlator $C^{\mathrm{CL}}(t)$ on 128^4 and 64^4 lattices using the same number of measurements. The straight line shows the expected volume scaling. (Right panel) Relative error of the vector-vector current correlator on 128^4 and 64^4 lattices in $a^{-1} = 2.33$ GeV and 160^4 lattice at $a^{-1} = 3.06$ GeV.

above the energy level of $2\sqrt{m_\pi^2 + (2\pi/L)^2}$ in the large t region on each ensemble. This is a clear indication of the existence of a lower energy state than the ρ meson mass in the region of $t \gtrsim 1$ fm, which is dominated by the multi-hadron state contributions.

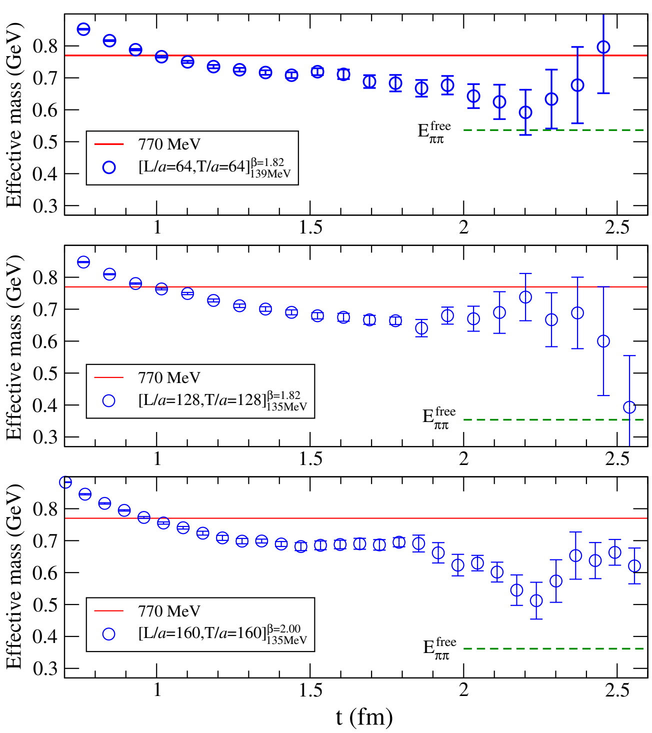

FIG. 2. Effective mass for the vector-vector current correlator at the physical pion mass on the (top panel) 64^4, (middle panel) 128^4, and (bottom panel) 160^4 lattices. Solid lines denote the physical ρ meson mass, and dashed ones are for the free two-pion energies $E_{\pi\pi}^{\mathrm{free}} = 2\sqrt{m_\pi^2 + (2\pi/L)^2}$ on each lattice volume.

IV. NUMERICAL RESULTS

With the use of the gauge field configurations explained in Sec. III, we perform a systematic study of uncertainties stemming from the FV effect, the cutoff effect, and the integration scheme dependence in the LQCD calculation of a_μ^{hvp}. For the FV effect, we directly compare the results for the coordinate-space integral of Eq. (18) obtained on the $L/a = 128$ and $L/a = 64$ lattices at the same cutoff scale of $a^{-1} = 2.33$ GeV. The cutoff effect is investigated by calculating the coordinate-space integral of Eq. (18) on the 128^4 and 160^4 lattices, keeping the physical lattice volume constant. We also discuss the operator dependence of the cutoff effect for the local and conserved vector currents. Finally we examine the consistency between the coordinate- and momentum-space integration schemes on the 128^4 [$(10.8\ \mathrm{fm})^4$] lattice at the physical pion mass.

A. Finite volume effect

Figure 3 shows the comparison of integrand in Eq. (18) between the $L/a = 128$ and $L/a = 64$ lattices. For the latter section, we extend T/a to 128 by copying the 64^4 lattice in the temporal direction so that we can eliminate the BPS wrapping around the temporal direction observed in our previous study [22] and discussed below. We remark that, although the 64^4 lattice configurations are generated at the same hopping parameter as for the 128^4 lattice, the measured pion mass $m_\pi = 139$ MeV on the 64^4 lattice is slightly heavier than $m_\pi = 135$ MeV on the 128^4 lattice due to the FV effect [23]. In the right panel of Fig. 3, one can see that the integrand has a clear tendency in which the magnitude of the integrand increases when L/a is enlarged from 64 to 128. The left panel of Fig. 4 plots the FV effect defined as

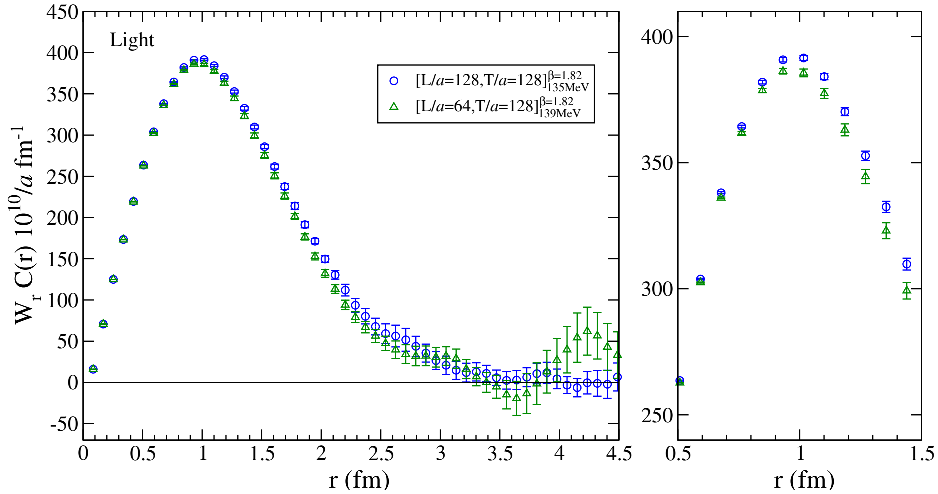

FIG. 3. Comparison of $C^{\mathrm{LL}}(r)W_r(r)$ in Eq. (18) between different spatial volumes with $L/a = 128$ and 64 in the light quark sector.

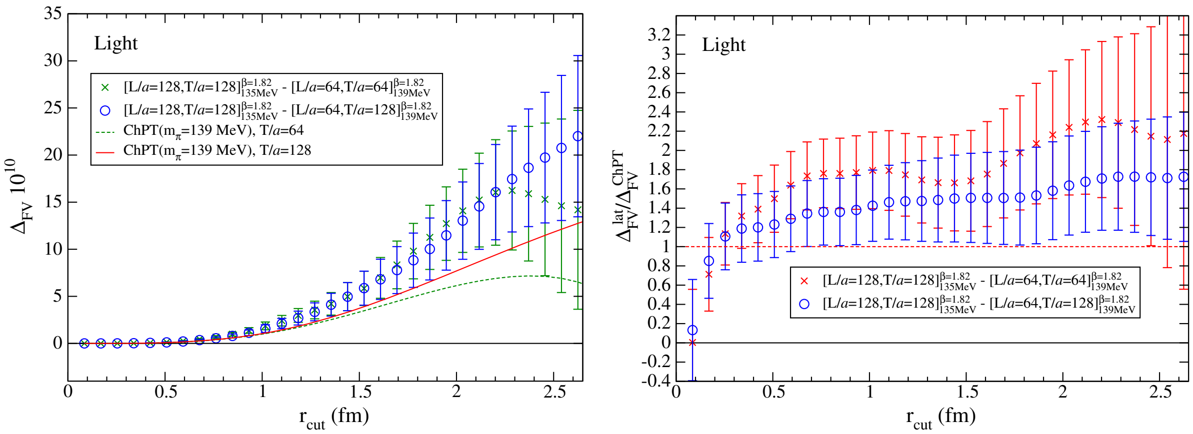

FIG. 4. (Left panel) Difference of $a_\mu^{\mathrm{hvp}}(r_{\mathrm{cut}})$ on the 128^4, 64^4, and $64^3 \times 128$ lattices in the light quark sector. The hopping parameters are the same on both lattices. The solid (dashed) curve denotes the leading order of the ChPT prediction for the FV effect between $(10.8\ \mathrm{fm})^3$ and $(5.4\ \mathrm{fm})^3$ spatial volumes with $m_\pi = 135$ MeV on the $[L/a = 128,\ T/a = 128]$ lattice, and 139 MeV on the $[L/a = 64,\ T/a = 128]$ ($[L/a = 64,\ T/a = 64]$) lattice. (Right panel) Ratio of the FV effect between the LQCD and ChPT estimates with the same symbol as the left panel.

$$\Delta_{\mathrm{FV}} = [a_\mu^{\mathrm{hvp}}(r_{\mathrm{cut}})]^l_{L/a=128} - [a_\mu^{\mathrm{hvp}}(r_{\mathrm{cut}})]^l_{L/a=64}, \tag{21}$$

which shows that the magnitude is larger than the leading-order ChPT, having the same sign as the ChPT prediction [19]. In this figure, we also make a comparison using the result for the 64^4 lattice. One can see that in the IR regime, larger than $r_{\mathrm{cut}} = 2.3$ fm, the BPS effect may be involved in FV correction as an enlarged a_μ^{hvp} effect on 64^4, and it then turns out to be additional systematic uncertainty. Use of the extended temporal direction as $64^3 \times 128$ thus plays an important role to avoid such a BPS effect from FV correction. In order to clarify the discrepancy, we plot the ratio of the FV effect between LQCD and ChPT at each r_{cut} in the right panel of Fig. 4. One can observe that the LQCD data tend to become larger than the ChPT prediction from $r \approx 1$ fm, and this tendency does not change even if r_{cut} increases, though the statistical error becomes larger.

The discrepancy of FV effect between LQCD and ChPT in the light quark sector is estimated as

$$\Delta_{\mathrm{FV}}^{\mathrm{lat}}/\Delta_{\mathrm{FV}}^{\mathrm{ChPT}} = \begin{cases} 2.16(66) & [\text{at } r_{\mathrm{cut}} \simeq 2.0 \text{ fm on } 64^4 \text{ lattice}], \\ 1.74(71) & [\text{at } r_{\mathrm{cut}} \simeq 2.6 \text{ fm on } 64^3 \times 128 \text{ lattice}], \end{cases} \tag{22}$$

on $L = 5.4$ fm at the physical pion mass. Comparing $T/a = 64$ and 128, as one can also see in Fig. 4, even at $r \simeq 2$ fm, there is a significant contribution of BPS regarded as an additional FV effect. Our result in Eq. (22) indicates that the actual FV effect tends to be larger than the

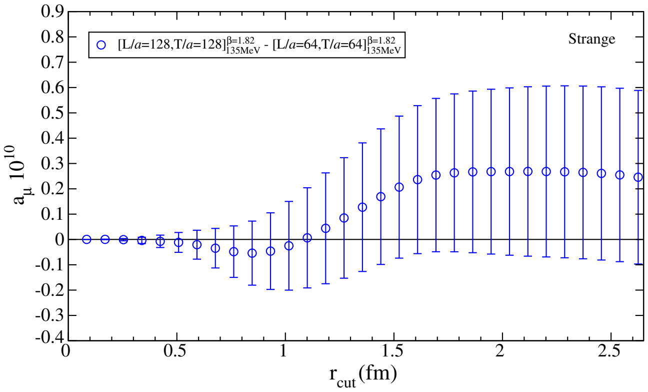

FIG. 5. Difference of $a_\mu^{\rm hvp}(r_{\rm cut})$ on the 128^4 and 64^4 lattices in the strange quark sector.

ChPT prediction, which may provide useful information on other recent LQCD results using ChPT or another analysis to correct the FV effect for $a_\mu^{\rm hvp}$ on (4 to 5 fm)^3 box [14,16–18].[4]

The similar analysis is made for the strange quark sector $[a_\mu^{\rm hvp}]^s$. Figure 5 shows little FV effect for $[a_\mu^{\rm hvp}]^s$, as expected from the fact that the strange quark mass is much heavier than the light one.

B. Cutoff effect

In Fig. 6, we plot $C^{\Gamma\Gamma'}(r)W_r(r)$ in Eq. (18) at two different cutoff scales of $a^{-1} = 2.33$ and 3.09 GeV on the same physical volume over $(10\ \text{fm})^4$ at the physical pion mass. We compare the cutoff effect in two types of vector-vector current correlators with $(\Gamma, \Gamma') = (\text{L, L})$ and (C, L) for the sink and source vector current operators in Eq. (20). We observe that $C^{\rm LL}(r)W_r(r)$ at different cutoff scales well agree with each other, whereas the sizable deviation is found for $C^{\rm CL}(r)W_r(r)$ from $r \simeq 0.5$ fm. Our LQCD results show that the $C^{\rm LL}(r)$ correlator has a smaller cutoff effect than the $C^{\rm CL}(r)$ one. In order to make a quantitative measurement of the discrepancy between the two types of the correlators, we plot the normalized difference defined as

$$\Delta_r(r) \equiv 1 - C^{\rm CL}(r)/C^{\rm LL}(r) \qquad (23)$$

in Fig. 7. The quantity shows a clear deviation from zero, and its magnitude is reduced for the finer lattice. Around $r \approx 1.5$ fm, we obtain

$$\Delta_r(r \approx 1.5\ \text{fm}) = \begin{cases} 0.089(3) & (a^{-1} = 2.33\ \text{GeV}) \\ 0.063(1) & (a^{-1} = 3.09\ \text{GeV}) \end{cases}, \qquad (24)$$

and their ratio $\Delta_r^{1/a=3.06\ \text{GeV}}/\Delta_r^{1/a=2.33\ \text{GeV}} = 0.71(3)$ is comparable to the cutoff ratio of $a^{-1}_{128^4}/a^{-1}_{160^4} = [2.333(18)\ \text{GeV}]/[3.089(30)\ \text{GeV}] = 0.76(1)$ (also see the right panel of Fig. 7). This suggests that the LQCD result with $C^{\rm CL}(r)$ is affected by the $\mathcal{O}(a)$ correction due to a significant cutoff effect on the conserved (point-splitting) current.

In Fig. 8, we plot the $r_{\rm cut}$ dependence for $[a_\mu^{\rm hvp}]_{\rm lat}(r_{\rm cut})$ in the light and strange quark sectors. They asymptotically reach constant values around $r_{\rm cut} \gtrsim 3.5$ fm without large statistical fluctuation. In both the light and strange quark sectors, $[a_\mu^{\rm hvp}]_{\rm lat}$ in the (L, L) channel at two cutoff scales agree within 1σ statistical error, while there is a 10% to 11% cutoff effect to affect $[a_\mu^{\rm hvp}]_{\rm lat}$ in the (C, L) channel at $a^{-1} = 2.33$ GeV.

We summarize the scaling properties for $[a_\mu^{\rm hvp}]^l_{\rm lat}$, $[a_\mu^{\rm hvp}]^s_{\rm lat}$, and $[a_\mu^{\rm hvp}]^c_{\rm lat}$ at two cutoff scales and their continuum extrapolations in Fig. 9, where the LQCD results at each cutoff scale are obtained by choosing $r_{\rm cut} \approx 3.5$ fm. One can see that the (L, L) channel has a rather small cutoff effect, which is not significant in the currently statistical precision, compared to the (C, L) channel in the light and strange quark sectors. Note that the local vector current we used here is not an $\mathcal{O}(a)$ improvement; however, in our lattice setup, the $\mathcal{O}(a)$ cutoff effect for the local current is automatically suppressed, and hence such an $\mathcal{O}(a)$ improvement is not required. This is expected in that the magnitude of c_A, which is the $\mathcal{O}(a)$ improvement factor for the local axial vector current, is almost zero when computed by the SF scheme [43] on the same lattice setup, and correspondingly c_V will be a similar order of magnitude. In addition, we check that the contribution of higher dimension operator $\bar{q}(\partial\sigma)_\mu q$, which is usually used for the $\mathcal{O}(a)$ improvement of the local vector current, is an order of magnitude smaller than that of the naive local vector current. On the other hand, for a conserved current without $\mathcal{O}(a)$ improvement, it is clear that the correction of the $\mathcal{O}(a)$ cutoff effect is needed to reduce the cutoff uncertainty even for our lattice setup. In our analysis, even though there are only two variations of lattice cutoff, it would be acceptable to use a constant fit of the (L, L) channel for $[a_\mu^{\rm hvp}]^l_{\rm lat}$ and $[a_\mu^{\rm hvp}]^s_{\rm lat}$ to take the continuum extrapolation, and we omit the (C, L) channel to avoid the additional systematic uncertainty due to a fitting with $\mathcal{O}(a)$ and a higher cutoff correction.

The systematic error is evaluated by taking the maximum difference between the central value obtained by the constant fit and the linearly extrapolated values in the (L, L) channels with the ansatz of the $\mathcal{O}(a)$ term, including the error of the lattice cutoff itself. The magnitude of the systematic error is comparable to that of the statistical one in the light and strange quark sectors. For the charm quark sector, the bottom panel of Fig. 9 shows the large cutoff

[4] $r_{\rm cut} \simeq 2.6$ fm is the maximum point of the window method in Ref. [17], and it then means that there still may be a large FV correction.

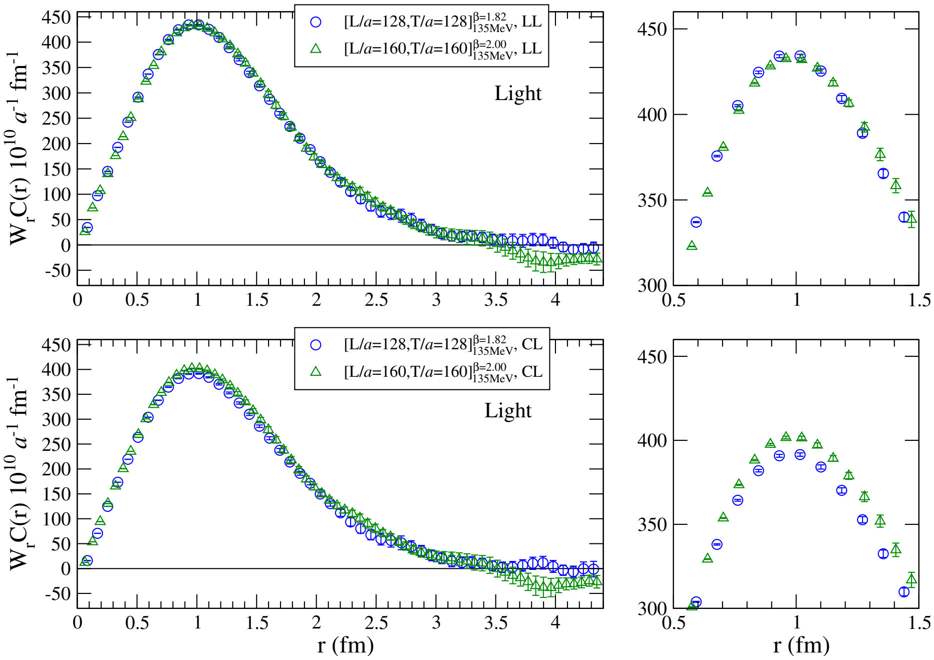

FIG. 6. (Top panels) $C^{\mathrm{LL}}(r)W_r(r)$ and (bottom panels) $C^{\mathrm{CL}}(r)W_r(r)$ in Eq. (18) in the light quark sector as a function of distance r on the 128^4 lattice at $a^{-1} = 2.33$ GeV (circles) and on the 160^4 lattice at $a^{-1} = 3.06$ GeV (triangles).

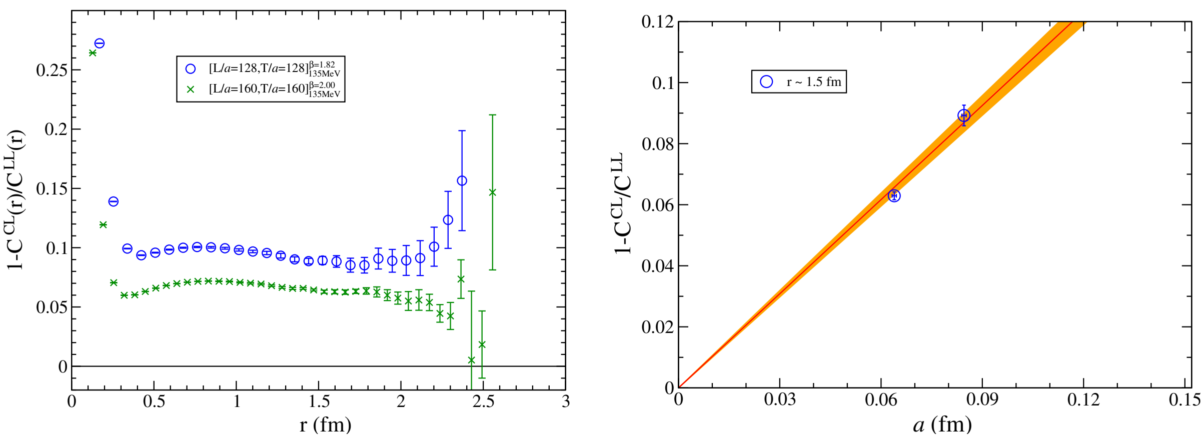

FIG. 7. (Left panel) r dependence of $\Delta_r(r) \equiv 1 - C^{\mathrm{CL}}(r)/C^{\mathrm{LL}}(r)$ on the 128^4 lattice at $a^{-1} = 2.33$ GeV (circles) and on the 160^4 lattice at 3.06 GeV (crosses). (Right panel) The cutoff dependence of $\Delta_r(r)$ at $r \simeq 1.5$ fm. The straight line and the band denote the central value and statistical error of the linear fitting function of $\Delta_r(r) \propto a$.

effect due to the $\mathcal{O}(am_c)$ contribution, even in the (L, L) channel. So we take the linearly extrapolated value in the (L, L) channel as the central value in the continuum limit, and its systematic error of the $\mathcal{O}(a^2)$ contribution is naively estimated as $(c_1 a)^2/c_0$, where c_1 is defined in the fit result of the linear extrapolation $c_0 + c_1 a$. Further analysis of the cutoff effect in the charm sector will be done by adding the data on one more fine lattice in the future. One can see that the uncertainty of the cutoff effect is dominant in the charm quark sector. For the total contribution of $[a_\mu^{\mathrm{hvp}}]^l_{\mathrm{lat}} + [a_\mu^{\mathrm{hvp}}]^s_{\mathrm{lat}} + [a_\mu^{\mathrm{hvp}}]^c_{\mathrm{lat}}$, the uncertainty in the light quark sector is still dominant.

C. Analysis of momentum-space integration scheme on 128^4 lattice

Compared to the coordinate-space integration scheme, the momentum-space integration scheme is rather straightforward for performing the integral in Eq. (1) once $\Pi(0)$ is determined by the zero-momentum extrapolation of the VPF [see Eq. (8)]. The advantage of this work over prior ones [15,30,49–51] is that we can not only access the VPF in the low-momentum region but also have high resolution in terms of Q^2 without resort to the twisted boundary condition for the valence quark by using a large lattice size larger than $(10\ \mathrm{fm})^4$. Our large lattice is also useful for

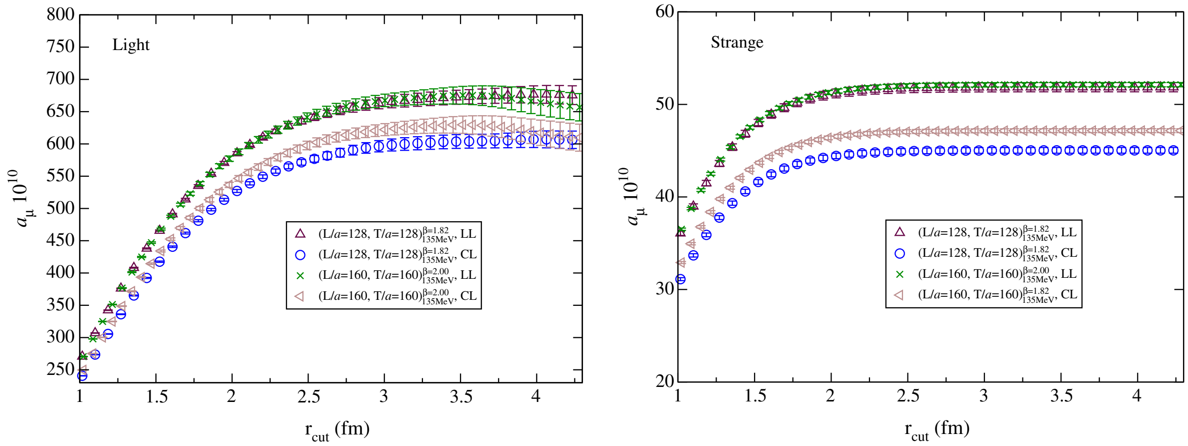

FIG. 8. LQCD results for $[a_\mu^{\mathrm{hvp}}]_{\mathrm{lat}}(r_{\mathrm{cut}})$ of Eq. (18) in the (L, L) and (C, L) channels on the 128^4 lattice at $a^{-1} = 2.33$ GeV, and on the 160^4 lattice at $a^{-1} = 3.09$ GeV. The left (right) panel pertains to the light (strange) quark sector.

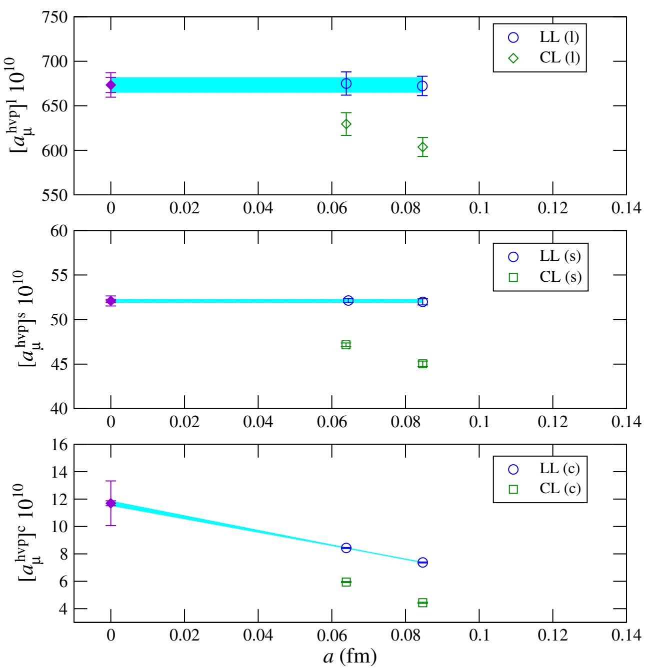

FIG. 9. Cutoff dependence of (top panel) $[a_\mu^{\mathrm{hvp}}]^l_{\mathrm{lat}}(r_{\mathrm{cut}})$, (middle panel) $[a_\mu^{\mathrm{hvp}}]^s_{\mathrm{lat}}(r_{\mathrm{cut}})$, and (bottom panel) $[a_\mu^{\mathrm{hvp}}]^c_{\mathrm{lat}}(r_{\mathrm{cut}})$ in the (L, L) and (C, L) channels with $r_{\mathrm{cut}} \approx 3.5$ fm. The extrapolated result in the continuum limit (diamond) has two kinds of errors: the inner one is statistical and the outer one denotes the total error, including the systematic error explained in the text.

reducing the uncertainty due to zero-momentum extrapolation and does not introduce the partially quenching effect for the different boundary conditions between the sea and valence quarks.

We plot the LQCD data of the VPF in each quark sector in Fig. 10, where the fit results of the Padé approximation of order [1,1] for the light and strange quark sectors using $Q^2_{\mathrm{fit}} \leq 0.05\ \mathrm{GeV}^2$ and the linear function for the charm quark using $Q^2_{\mathrm{fit}} \leq 0.065\ \mathrm{GeV}^2$ are also shown. We observe that the VPFs in the light and strange quark sectors have stronger slope around the zero-momentum region than in the charm quark sector. As shown in Fig. 10, the Padé approximation of lowest order of [1, 1] well describes such a lattice data with reasonable $\chi^2/\mathrm{dof} < 1$ in the correlated fit. Although we employ a narrow fit range close to zero momentum, Fig. 11 shows that the fit function agrees with the Q^2 dependence of the LQCD data up to $Q^2 = 0.4\ \mathrm{GeV}^2$, which is far beyond the fitting range. This behavior indicates that the lowest Padé approximation, which consists of single pole dominance, is a reasonable approximation in the IR regime. Since the VPF multiplied by the weight function W_q in $Q^2 \geq 0.5\ \mathrm{GeV}^2$ gives a tiny contribution to the total a_μ^{hvp}, as mentioned in Sec. II A, we evaluate the integral without the PQCD part [the third term of Eq. (8)] in our analysis. In fact, the LQCD data of integrals larger than $Q^2 \approx 0.5\ \mathrm{GeV}^2$ are below 0.5×10^{-10}, corresponding to less than 0.1% for a_μ^{hvp} (see the right panel of Fig. 11), and it is then negligible. Therefore we hereafter estimate a_μ^{hvp} using integrals up to $Q^2 = 0.5\ \mathrm{GeV}^2$.

Since the integrand has a sharp peak structure significantly below the minimum momentum squared $Q^2_{\mathrm{min}} \approx 0.013\ \mathrm{GeV}^2$ allowed for our ensemble (see Fig. 11), the integral in Eq. (8) is sensitive to the extrapolation procedure from Q^2_{min} to zero. We employ the linear extrapolation and the Padé approximation of order [1,1] and [2,1]. Figure 12 compares the results of $[a_\mu^{\mathrm{hvp}}]_{\mathrm{Mom}}$ obtained by both extrapolation methods while varying the fitting ranges from Q^2_{min} to Q^2_{fit}. In the case of linear extrapolation, the results of $[a_\mu^{\mathrm{hvp}}]_{\mathrm{Mom}}$ show significant Q^2_{fit} dependence due to a higher-order term than $\mathcal{O}(Q^2)$ even in $Q^2 \approx 0.013\ \mathrm{GeV}^2$, except for the charm quark sector. On the other hand, we observe little Q^2_{fit} dependence for $[a_\mu^{\mathrm{hvp}}]_{\mathrm{Mom}}$ with the Padé approximation of order [1,1] and [2,1] up to $Q^2_{\mathrm{fit}} = 0.235\ \mathrm{GeV}^2$ in

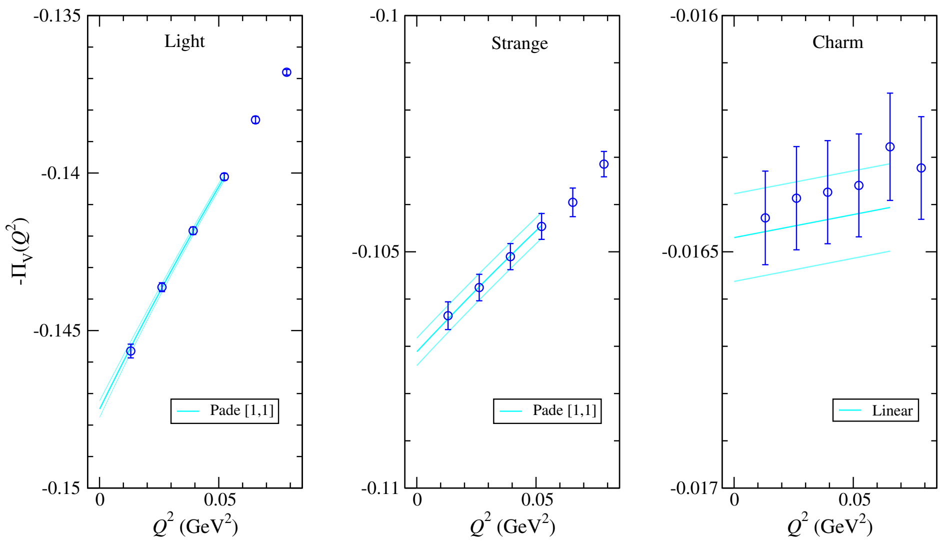

FIG. 10. Q^2 dependence of the VPF in (left panel) light, (middle panel) strange, and (right panel) charm quark sectors. Solid lines denote the fit results, including the statistical error with (left and middle panels) the Padé [1,1] approximation and (right panel) the linear function.

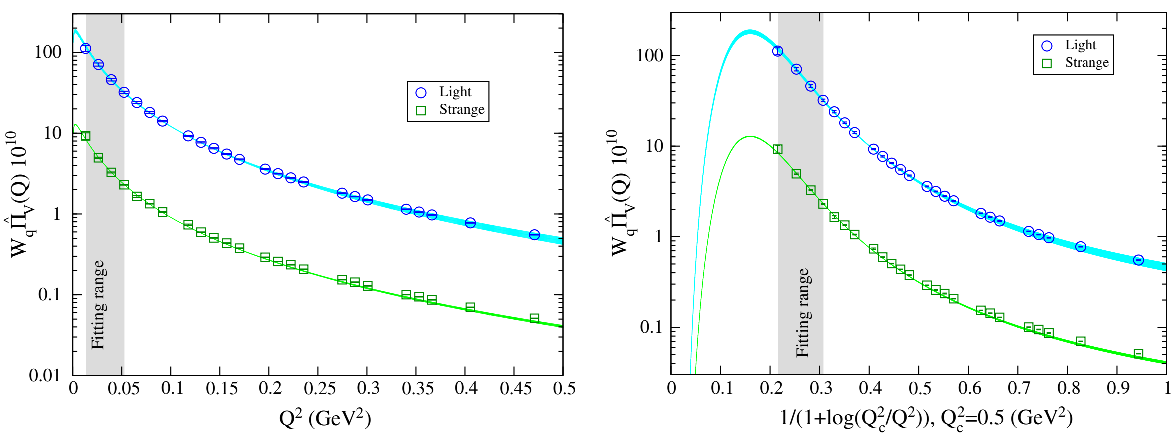

FIG. 11. Q^2 dependence of the integrand in Eq. (1) up to $Q^2 = 0.5$ GeV^2 at the light and strange quark sectors. The horizontal axis is rescaled to a dimensionless quantity $1/(1 + \ln(Q_c^2/Q^2))$ [52] with $Q_c^2 = 0.5$ GeV^2 in the right panel. Curved bands show the fit results including the statistical error. The shaded vertical band denotes the fitting range for $\Pi(Q)$.

the light quark sector. We find that, even with different $Q^2_{\rm fit}$ and different orders of Padé approximation, the result in the momentum-space integration scheme is in good agreement with $[a_\mu^{\rm hvp}]^{\rm CL}_{\rm lat}(r_{\rm cut})$ at $r_{\rm cut} = 3.5$ fm within 1.5σ error, and this is thus a consistency test for the scheme independence. We also find that the systematic uncertainty due to fitting with the Padé approximation is negligible in our study on the $L = 10.8$ fm lattice.

Here we notice the strong $Q^2_{\rm fit}$ dependence for the results in the strange quark sector that appear in Fig. 12. In this case, an extra lattice cutoff effect of $\mathcal{O}(am_s(aQ)^2)$, which is not described by the naive Padé approximation, may arise in the strange quark sector. More detailed study will be needed in the future.

In contrast to the 128^4 lattice, Fig. 13 shows the significant $Q^2_{\rm fit}$ dependence for the results with both extrapolation methods on the 64^4 lattice since the low Q^2 data has coarse resolution on this lattice. Our LQCD study suggests that the lattice size with $L = 5.4$ fm at the physical pion mass, corresponding to $m_\pi L = 3.8$, is not large enough for the momentum-space integration scheme to obtain a reliable result of $a_\mu^{\rm hvp}$ because of large FV correction.

We remark that the statistical precision of the result for $[a_\mu^{\rm hvp}]_{\rm Mom}$ is more easily obtained than that for $[a_\mu^{\rm hvp}]_{\rm lat}$. This is because of a noise cancellation in $\hat{\Pi}(Q)$ between the extrapolated $\Pi(0)$ and $\Pi(Q)$, which are highly correlated with each other. In addition, in the momentum-space integration scheme, we do not need to introduce the truncation of the integration range corresponding to the IR truncation $r_{\rm cut}$ in the coordinate-space integration scheme. This indicates the possibility that once we have

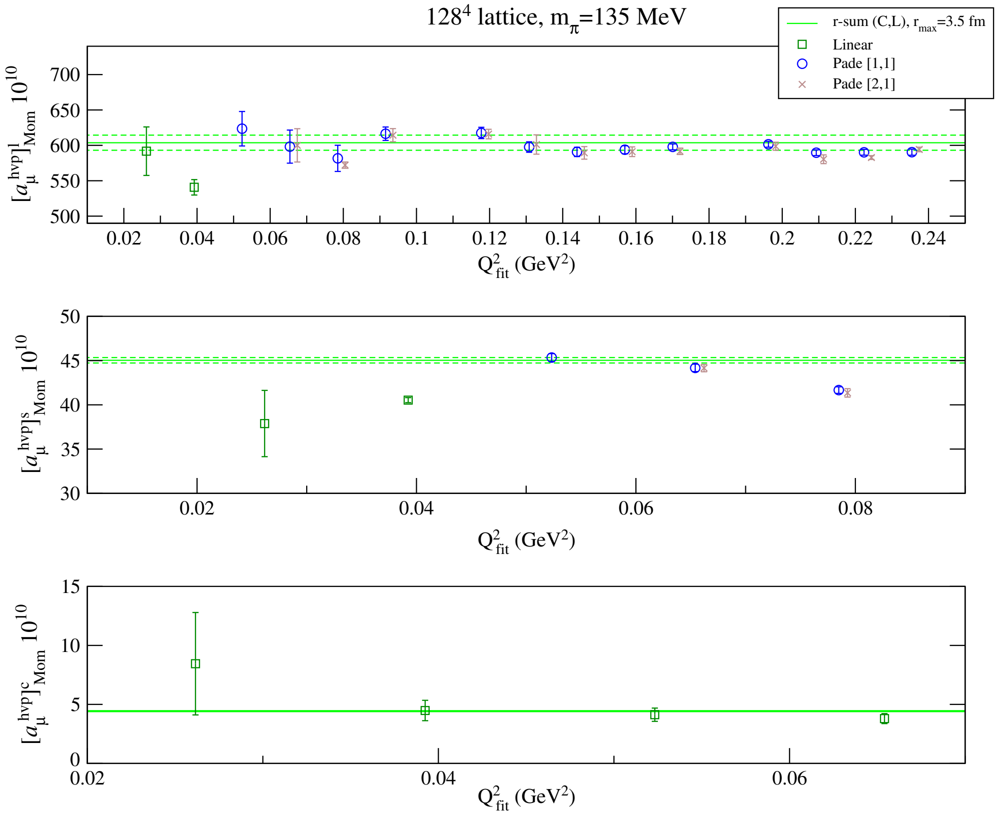

FIG. 12. $Q^2_{\rm fit}$ dependence in zero-momentum extrapolation with linear function and Padé approximation for the VPF in (top panel) light, (middle panel) strange, and (bottom panel) charm quark sectors. The horizontal lines are the central value (solid) and statistical error (dashed) of the result in the coordinate-space integration scheme with $r_{\rm cut} \approx 3.5$ fm.

low Q^2 data covering a peak position of W_q ($Q^2 \sim 0.003$ GeV^2), for which we need to prepare a box size 2 times larger than in this study, we can obtain a high precision result with smaller statistical and systematic errors than the coordinate-space integration scheme.

D. Discussion

We obtain the connected $a_\mu^{\rm hvp}$ in the light, strange, and charm quark sectors at the physical point:

$$a_\mu^{\rm hvp} = \begin{cases} 673(9)(11) \times 10^{-10} & [\text{light}] \\ 52.1(2)(5) \times 10^{-10} & [\text{strange}], \\ 11.7(2)(1.6) \times 10^{-10} & [\text{charm}] \end{cases} \qquad (25)$$

where the first error is statistical for $(\Gamma, \Gamma') = (\mathrm{L}, \mathrm{L})$ with the constant fit, and the second one is systematic for the uncertainty in the continuum extrapolation explained in Sec. IV B. We find that the statistical and systematic errors for the light quark sector gives the leading contribution to

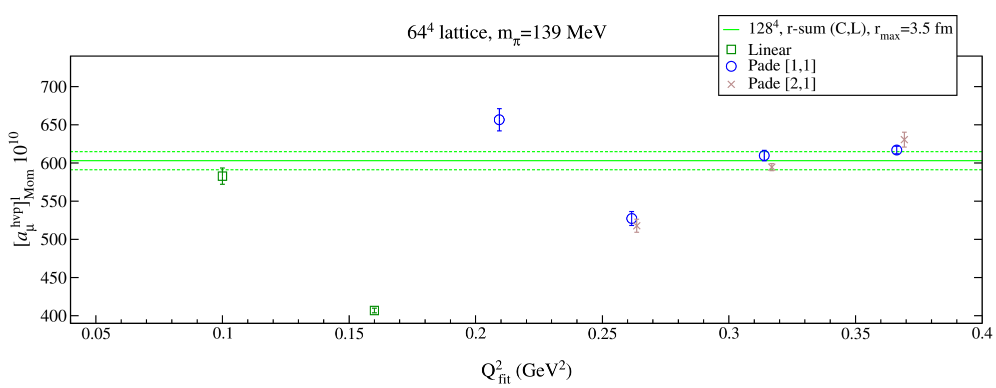

FIG. 13. The same as Fig. 12 but on a 64^4 lattice.

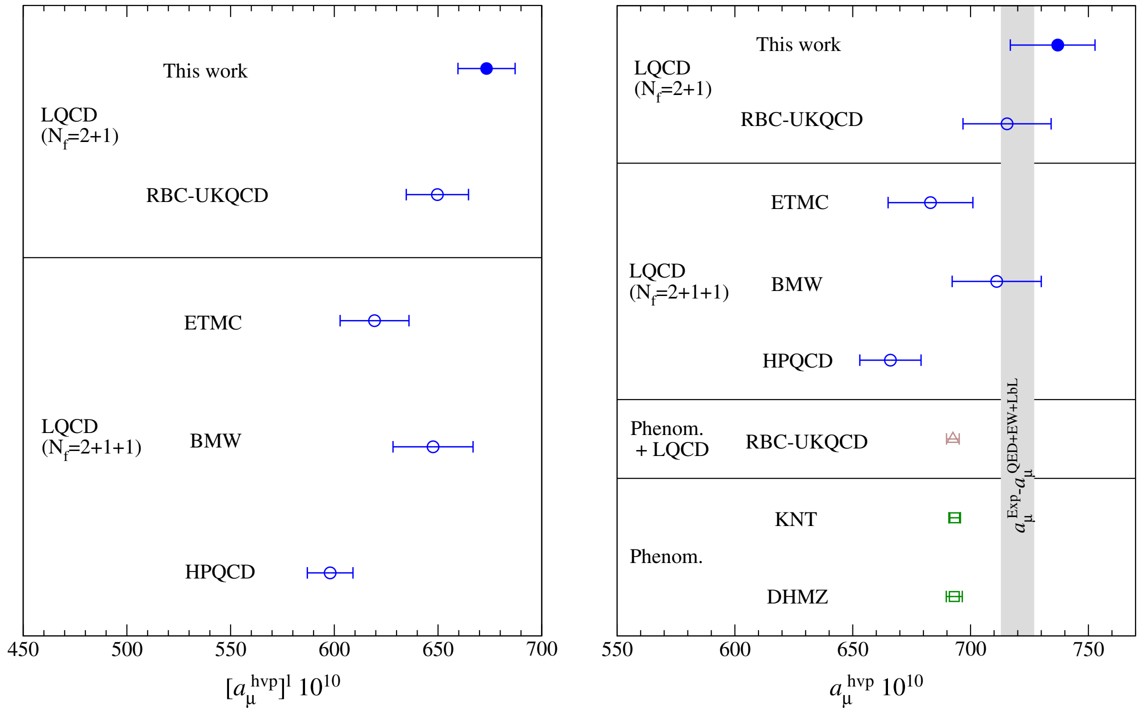

FIG. 14. (Left panel) Summary plot of the connected $a_\mu^{\rm hvp}$ in the light quark sector $[a_\mu^{\rm hvp}]^l$ and (right panel) the full result of $a_\mu^{\rm hvp}$ in comparison with recent LQCD results ($N_f \geq 3$) of the BMW [16], ETMC [18], HPQCD [14], and RBC-UKQCD [17] collaborations, and phenomenological estimate obtained with the experimental R-ratio by DHMZ [10] and KNT [11]. The shaded vertical band shows the experimental $a_\mu^{\rm hvp}$ estimated as the difference between the BNL experimental value of a_μ and the theoretical value with QED and EW, including the light-by-light scattering contribution. The error bar for $[a_\mu^{\rm hvp}]^l$ in this work represents the combined error with the statistical one and the systematic one due to the cutoff effect. Additional uncertainties of the missing disconnected diagram and the IB effect are included in the error bar of $a_\mu^{\rm hvp}$ in this work.

the total error. The contributions from the strange and charm quark sectors are minor effects.

Here we make two remarks:

(1) Our choice of $r_{\rm cut} \approx 3.5$ fm in the coordinate-space integration scheme, which is larger than the 3 fm value employed in Refs. [16,17], is large enough to control the IR truncation. In Figs. 6 and 8, we observe that the integrand has a nonzero value of $23(10) \times 10^{-10}$ at $r_{\rm cut} \approx 3$ fm in the $(\Gamma, \Gamma') = (\mathrm{L}, \mathrm{L})$ channel on the 128^4 lattice, and the integral is still increasing, while the integrand is consistent with zero at $r_{\rm cut} \approx 3.5$ fm, and the integral does not depend on $r_{\rm cut}$ even if we use a larger $r_{\rm cut}$. High precision data on a lattice larger than $(10\ \mathrm{fm})^4$ at the physical point allow us to evaluate the integral with the IR truncation effect under control.

(2) The scaling properties presented in Sec. IV B are similar to the domain-wall fermion case [17], though the computational cost is much lower for Wilson-type quark action. The continuum extrapolation is straightforward and theoretically robust for Wilson-type quark action compared to the staggered fermion case [16,53].

In this paper, we concentrate on the connected HVP diagram, while there are some missing diagrams of the isoscalar contribution with the disconnected diagram and the isospin breaking (IB) term due to the QED correction. Referring to the recent work in Refs. [16,17], we conservatively add the systematic error of the quark disconnected diagram contribution as a -2% effect, and the IB effect as a $+1\%$ error to the total contribution. We then find that

$$a_\mu^{\rm hvp} = 737(9)(^{+13}_{-18}) \times 10^{-10}, \tag{26}$$

where the first error is statistical and the second one represents the total systematic error obtained in the quadrature. The magnitude of the error is still 2.7%, in which the systematic error, mainly due to the uncertainty of disconnected diagram, is more than 2 times larger than the statistical one. Compared to other lattice results ($N_f \geq 3$) (see Fig. 14), our value is consistent with the results by the RBC-UKQCD [17] and BMW [16] collaborations, while we find slight tension with recent results of the ETMC [18] and HPQCD [14] collaborations, and 2σ deviation from the phenomenological estimates [10,11]. Our result seems to favor the "experimental" $a_\mu^{\rm hvp}$, which is defined as the difference between the BNL experimental value of a_μ and the theoretical calculation with QED and electroweak gauge symmetry (EW), including the light-by-light scattering contribution in Ref. [12].

V. SUMMARY

We have studied the systematic uncertainties in the LQCD calculation of $a_\mu^{\rm hvp}$ on PACS10 gauge configurations which have a greater than $(10\ {\rm fm})^4$ box size at the physical point with two different lattice cutoffs. This study and a previous work [22] are the direct LQCD calculations without use of any ansatz or reliance on any effective models. The optimized LQCD calculation of HVP on a sufficiently large lattice size at the physical point allows us to access the deep IR regime where the contributions of multihadron states become manifest. Our study points out that such contributions may be larger than the estimate in the leading order of ChPT. In Fig. 14, we observe that our result of $a_\mu^{\rm hvp}$ is relatively larger than that of other LQCD studies. The reason for such a tendency may be due to the discrepancy between LQCD and ChPT (or related phenomenological models) including only a two-pion state contribution, which was applied to evaluate the FV correction in other LQCD studies, as discussed in Sec. IV A. We have also investigated the lattice cutoff effect in the coordinate-space integration scheme using data at two different cutoffs. We find that the cutoff effect is tamed for the local vector current on our gauge configurations. Furthermore, the momentum-space integration scheme on a $L > 10$ fm lattice yields high quality data for a VPF close to $Q^2 = 0$, which substantially reduces uncertainty in the zero-momentum extrapolation. With a careful study of the extrapolation procedure dependence, we have confirmed the consistency between the results in the momentum- and coordinate-space integration schemes.

The total error for the result of $a_\mu^{\rm hvp}$ is 2.7%, of which the statistical error is 1.2% and the remaining is the systematic uncertainty. We plan to reduce both the statistical and systematic errors with additional calculations, including one finer lattice, disconnected diagram, and QED effect in the future. Here we will point out the possibility that the momentum-space integration scheme with $L > 20$ fm covers the peak position of kernel function in the low Q^2 regime, so it could be a rigorous test for the LQCD scheme. We leave that for future work.

ACKNOWLEDGMENTS

We would like to thank Taku Izubuchi and Christoph Lehner, and also PACS Collaboration members, for the helpful discussion and support. The computation code was developed based on Columbia Physics System (CPS), incorporating the optimized OpenQCD system.[5] This work is supported in part by the U.S.-Japan Science and Technology Cooperation Program in High Energy Physics for FY2018, Interdisciplinary Computational Science Program of Center for Computational Sciences (CCS), at the University of Tsukuba, general use No. G18001 at ACCC, and the HPCI System Research project (Project IDs No. hp180126 and No. hp190068). Numerical calculations were performed on the K computer at the RIKEN Center for Computational Science (R-CCS), on Hokusai at the Advanced Center for Computing and Communication (ACCC) in RIKEN, on XC40 at YITP in Kyoto University, on the Fujitsu PRIMERGY CX600M1/CX1640M1 (Oakforest-PACS) at the Information Technology Center, The University of Tokyo, and on the computer facilities at the Research Institute for Information Technology, Kyushu University.

[5]See http://luscher.web.cern.ch/luscher/openQCD/.

APPENDIX: THE DERIVATION OF COORDINATE REPRESENTATION

The Fourier transformation of Eq. (14) is defined as

$$G(Q) = \int d^4x e^{iQx} C(x) = 3Q^2 \Pi(Q). \qquad \text{(A1)}$$

$\hat{\Pi}$ in Eq. (2) can be represented as

$$\hat{\Pi}(\omega) = \frac{1}{3\omega^2} G(\omega) - \frac{1}{3\omega^2} G(\omega)\bigg|_{\omega=0}, \qquad \text{(A2)}$$

where the second term is expanded as

$$\frac{1}{3\omega^2} G(\omega)\bigg|_{\omega=0} = \frac{1}{3\omega^2}\left[G(0) + \frac{1}{2}\omega^2 G''(0) + \mathcal{O}(\omega^4)\right], \qquad \text{(A3)}$$

and we obtain

$$\hat{\Pi}(\omega) = \frac{1}{3\omega^2} G(\omega) - \frac{1}{3\omega^2} G(0) - \frac{1}{6} G''(0). \qquad \text{(A4)}$$

In general, the second derivative of G with respect to $\omega = |Q|$ can be expressed as

$$G''(\omega) = \int d^4x e^{iQx}\left[\sum_{\mu\nu}(-x_\mu x_\nu)\frac{\omega^2}{Q_\mu Q_\nu} e^{iQx} C(x)\bigg|_{Q_\mu\neq 0, Q_\nu \neq 0}\right]_{\omega=|Q|}, \qquad \text{(A5)}$$

where the terms with odd power of x_μ vanish in the coordinate integral. By substituting the above equation into Eq. (1), we can obtain Eq. (15).

[1] G. W. Bennett *et al.* (Muon $g-2$ Collaboration), Phys. Rev. Lett. **92**, 161802 (2004).
[2] G. W. Bennett *et al.* (Muon $g-2$ Collaboration), Phys. Rev. D **73**, 072003 (2006).
[3] D. Flay (Muon $g-2$ Collaboration), in *Proceedings of the 38th International Conference on High Energy Physics (ICHEP 2016), Chicago, 2016* [Proc. Sci., ICHEP2016 (**2017**) 1075].
[4] K. Shimomura, Hyperfine Interact. **233**, 89 (2015).
[5] M. Lindner, M. Platscher, and F. S. Queiroz, Phys. Rep. **731**, 1 (2018).
[6] M. Gourdin and E. De Rafael, Nucl. Phys. **B10**, 667 (1969).
[7] M. Davier, A. Hoecker, B. Malaescu, and Z. Zhang, Eur. Phys. J. C **71**, 1515 (2011); **72**, 1874(E) (2012).
[8] K. Hagiwara, R. Liao, A. D. Martin, D. Nomura, and T. Teubner, J. Phys. G **38**, 085003 (2011).
[9] F. Jegerlehner, EPJ Web Conf. **118**, 01016 (2016).
[10] M. Davier, A. Hoecker, B. Malaescu, and Z. Zhang, Eur. Phys. J. C **77**, 827 (2017).
[11] A. Keshavarzi, D. Nomura, and T. Teubner, Phys. Rev. D **97**, 114025 (2018).
[12] C. Patrignani *et al.* (Particle Data Group), Chin. Phys. C **40**, 100001 (2016).
[13] H. B. Meyer and H. Wittig, Prog. Part. Nucl. Phys. **104**, 46 (2019).
[14] B. Chakraborty, C. T. H. Davies, P. G. de Oliviera, J. Koponen, and G. P. Lepage, Phys. Rev. D **96**, 034516 (2017).
[15] M. Della Morte, A. Francis, V. Gülpers, G. Herdoíza, G. von Hippel, H. Horch, B. Jäger, H. B. Meyer, A. Nyffeler, and H. Wittig, J. High Energy Phys. 10 (2017) 020.
[16] S. Borsanyi *et al.* (Budapest-Marseille-Wuppertal Collaboration), Phys. Rev. Lett. **121**, 022002 (2018).
[17] T. Blum, P. A. Boyle, V. Gülpers, T. Izubuchi, L. Jin, C. Jung, A. Jüttner, C. Lehner, A. Portelli, and J. T. Tsang, Phys. Rev. Lett. **121**, 022003 (2018).
[18] D. Giusti, F. Sanfilippo, and S. Simula, Phys. Rev. D **98**, 114504 (2018).
[19] C. Aubin, T. Blum, P. Chau, M. Golterman, S. Peris, and C. Tu, Phys. Rev. D **93**, 054508 (2016).
[20] M. Golterman, K. Maltman, and S. Peris, Phys. Rev. D **95**, 074509 (2017).
[21] J. Bijnens and J. Relefors, J. High Energy Phys. 12 (2017) 114.
[22] T. Izubuchi, Y. Kuramashi, C. Lehner, and E. Shintani (PACS Collaboration), Phys. Rev. D **98**, 054505 (2018).
[23] K. I. Ishikawa, N. Ishizuka, Y. Kuramashi, Y. Nakamura, Y. Namekawa, Y. Taniguchi, N. Ukita, T. Yamazaki, and T. Yoshie (PACS Collaboration), Phys. Rev. D **99**, 014504 (2019).
[24] B. E. Lautrup, A. Peterman, and E. de Rafael, Phys. Rep. **3**, 193 (1972).
[25] E. Shintani, S. Aoki, T. W. Chiu, S. Hashimoto, T. H. Hsieh, T. Kaneko, H. Matsufuru, J. Noaki, T. Onogi, and N. Yamada (JLQCD and TWQCD Collaborations), Phys. Rev. D **79**, 074510 (2009).
[26] E. Shintani, S. Aoki, H. Fukaya, S. Hashimoto, T. Kaneko, T. Onogi, and N. Yamada (JLQCD collaboration), Phys. Rev. D **82**, 074505 (2010).
[27] R. J. Hudspith, R. Lewis, K. Maltman, and E. Shintani, arXiv:1804.10286.
[28] P. A. Baikov, K. G. Chetyrkin, and J. H. Kuhn, Phys. Rev. Lett. **101**, 012002 (2008).
[29] E. Braaten, S. Narison, and A. Pich, Nucl. Phys. **B373**, 581 (1992).
[30] C. Aubin, T. Blum, M. Golterman, and S. Peris, Phys. Rev. D **86**, 054509 (2012).
[31] D. Bernecker and H. B. Meyer, Eur. Phys. J. A **47**, 148 (2011).
[32] H. B. Meyer, Eur. Phys. J. C **77**, 616 (2017).
[33] Y. Iwasaki, arXiv:1111.7054.
[34] Y. Taniguchi, Proc. Sci., LATTICE2012 (**2012**) 236 [arXiv:1303.0104].
[35] K.-I. Ishikawa, N. Ishizuka, Y. Kuramashi, Y. Nakamura, Y. Namekawa, E. Shintani, Y. Taniguchi, N. Ukita, T. Yamazaki, and T. Yoshi (PACS Collaboration), arXiv:1907.10846
[36] M. Luscher, J. High Energy Phys. 05 (2003) 052.
[37] M. Luscher, Comput. Phys. Commun. **165**, 199 (2005).
[38] M. Hasenbusch, Phys. Lett. B **519**, 177 (2001).
[39] M. Hasenbusch and K. Jansen, Nucl. Phys. **B659**, 299 (2003).
[40] S. Aoki *et al.* (PACS-CS Collaboration), Phys. Rev. D **79**, 034503 (2009).
[41] J. C. Sexton and D. H. Weingarten, Nucl. Phys. **B380**, 665 (1992).
[42] M. A. Clark and A. D. Kennedy, Phys. Rev. Lett. **98**, 051601 (2007).
[43] K. I. Ishikawa, N. Ishizuka, Y. Kuramashi, Y. Nakamura, Y. Namekawa, Y. Taniguchi, N. Ukita, T. Yamazaki, and T. Yoshi (PACS Collaboration), Proc. Sci., LATTICE2015 (**2016**) 271 [arXiv:1511.08549].
[44] E. Shintani, K.-I. Ishikawa, Y. Kuramashi, S. Sasaki, and T. Yamazaki, Phys. Rev. D **99**, 014510 (2019).
[45] T. Blum, T. Izubuchi, and E. Shintani, Phys. Rev. D **88**, 094503 (2013).
[46] E. Shintani, R. Arthur, T. Blum, T. Izubuchi, C. Jung, and C. Lehner, Phys. Rev. D **91**, 114511 (2015).
[47] G. von Hippel, T. D. Rae, E. Shintani, and H. Wittig, Nucl. Phys. **B914**, 138 (2017).
[48] M. Luscher, J. High Energy Phys. 07 (2007) 081.
[49] M. Della Morte, B. Jager, A. Juttner, and H. Wittig, J. High Energy Phys. 03 (2012) 055.
[50] C. Aubin, T. Blum, M. Golterman, and S. Peris, Phys. Rev. D **88**, 074505 (2013).
[51] F. Burger, X. Feng, G. Hotzel, K. Jansen, M. Petschlies, and D. B. Renner (ETM Collaboration), J. High Energy Phys. 02 (2014) 099.
[52] P. Boyle, L. Del Debbio, E. Kerrane, and J. Zanotti, Phys. Rev. D **85**, 074504 (2012).
[53] S. Borsanyi, Z. Fodor, T. Kawanai, S. Krieg, L. Lellouch, R. Malak, K. Miura, K. K. Szabo, C. Torrero, and B. Toth, Phys. Rev. D **96**, 074507 (2017).